



**HAL**  
open science

## Photon tunneling reconstitution in black phosphorus/hBN heterostructure

Cheng-Long Zhou, Yong Zhang, Zahra Torbatian, Dino Novko, Mauro Antezza, Hong-Liang Yi

► **To cite this version:**

Cheng-Long Zhou, Yong Zhang, Zahra Torbatian, Dino Novko, Mauro Antezza, et al.. Photon tunneling reconstitution in black phosphorus/hBN heterostructure. *Physical Review Materials*, 2022, 6, pp.075201. 10.1103/PhysRevMaterials.6.075201 . hal-03739127

**HAL Id: hal-03739127**

**<https://hal.science/hal-03739127v1>**

Submitted on 13 Jun 2024

**HAL** is a multi-disciplinary open access archive for the deposit and dissemination of scientific research documents, whether they are published or not. The documents may come from teaching and research institutions in France or abroad, or from public or private research centers.

L'archive ouverte pluridisciplinaire **HAL**, est destinée au dépôt et à la diffusion de documents scientifiques de niveau recherche, publiés ou non, émanant des établissements d'enseignement et de recherche français ou étrangers, des laboratoires publics ou privés.

## Photon tunneling reconstitution in black phosphorus/*h*BN heterostructure

Cheng-Long Zhou,<sup>1,2</sup> Yong Zhang<sup>1,2</sup>, Zahra Torbatian,<sup>3</sup> Dino Novko<sup>4,5</sup>, Mauro Antezza<sup>6,7</sup> and Hong-Liang Yi<sup>1,2,\*</sup>

<sup>1</sup>*School of Energy Science and Engineering, Harbin Institute of Technology, Harbin 150001, People's Republic of China*

<sup>2</sup>*Key Laboratory of Aerospace Thermophysics, Ministry of Industry and Information Technology, Harbin 150001, People's Republic of China*

<sup>3</sup>*School of Nano Science, Institute for Research in Fundamental Sciences (IPM), Tehran 19395-5531, Iran*

<sup>4</sup>*Institute of Physics, Zagreb 10000, Croatia*

<sup>5</sup>*Donostia International Physics Center (DIPC), Donostia-San Sebastián 20018, Spain*

<sup>6</sup>*Laboratoire Charles Coulomb (L2C), Unité mixte de recherche (UMR) 5221 Centre national de la recherche scientifique (CNRS), Université de Montpellier, F-34095 Montpellier, France*

<sup>7</sup>*Institut Universitaire de France, 1 rue Descartes, F-75231 Paris, France*



(Received 28 March 2022; revised 25 June 2022; accepted 7 July 2022; published 26 July 2022)

Excitation of hybrid modes constituted by different material-supported polaritons is a common way to enhance the near-field radiative energy transport, which has fascinating promise in applications of thermal photonics. Here, we investigate near-field thermal radiation mechanisms in heterostructure composed of *h*BN film and black phosphorus single layer. The results show that this heterostructured system can give rise to a remarkable enhancement for photon tunneling, outperforming the near-field thermal radiation properties of its building blocks, as well as some other representative heterostructures. Moreover, we find that the anisotropic hybrid effect can induce a remarkable topological reconstitution of polaritons for *h*BN film and black phosphorus, forming a novel anisotropic hybrid polaritons. Notably, such hybrid modes show significant topological differences compared to *h*BN film and black phosphorus in the type-I Reststrahlen band due to the anisotropic anticrossing hybridization effect. Lastly, we systematically analyze the evolution of such hybrid polariton modes as a function of *h*BN film thickness and the corresponding influence on radiative properties of the heterostructure. This work may benefit the applications of near-field energy harvesting and radiative cooling based on hybrid polaritons in anisotropic two-dimensional material and hyperbolic film.

DOI: [10.1103/PhysRevMaterials.6.075201](https://doi.org/10.1103/PhysRevMaterials.6.075201)

### I. INTRODUCTION

Compared with classical radiation [1,2], evanescent waves coupling between two bodies with subwavelength separation distances can assist photons to tunnel through the vacuum gap (i.e., photon tunneling), resulting in radiative heat flux (RHF) that can exceed the blackbody limit by several orders of magnitude [3,4]. This is the so-called near-field thermal radiation (NFTR). During the last two decades, this colossal enhancement of thermal radiation has inspired a lot of research interest for its fundamental scientific relevance [5–7] and turned out to be particularly important for technological applications, such as thermal logic circuitry [8–12], near-field thermophotovoltaics [13–15], photon transformers [16], and photonic cooling [17–19]. To benefit these potential applications, continuous efforts have been devoted to explore polariton modes that could intensify photon tunneling and thermal radiation. Prominent examples include surface phonon polaritons supported by polar dielectric materials such as SiO<sub>2</sub> and SiC [20–24] or surface plasmon polaritons (SPPs) that can exist at the surface of semiconductors and noble metals [25–29]. Additionally, recent advances have witnessed that hybridization of different kinds of polaritons provides an exciting paradigm to further boost NFTR [30–37]. Researchers have found that

the SPPs of graphene can couple with the multiple hyperbolic waveguide modes of the hyperbolic film to produce a fascinating dispersion behavior, which can modulate photon tunneling and provide substantial enhancement of thermal radiation on the nanoscale [38]. Inspired by this concept, many interesting ideas have been put forward in recent years, and the interested reader can consult the recent reviews of Refs. [39–45]. However, the isofrequency contour of SPPs of graphene is a closed circle, so the density of states (DOS) is finite, preventing further enhancement of photon tunneling and NFTR [46–48].

As the technology of metamaterial fabrication develops, authors of extensive studies have shown that, compared with graphene, anisotropic two-dimensional (2D) materials are an ideal platform for enhancing NFTR due to their higher DOS around the plasmon frequency [49–51]. A prominent example of such anisotropic 2D materials is a single layer of black phosphorus (BP) or phosphorene doped with excess charge, for which RHF exceeds that of optimized graphene sheets by at least 18.5% [49]. Therefore, combining anisotropic 2D materials with the hyperbolic waveguide mode of hyperbolic films to form hybrid polariton modes appears to be a promising pathway for improving NFTR [52]. However, unlike graphene, anisotropic 2D materials would be subject to stronger anisotropy-oriented hybridization from hyperbolic waveguide modes of hyperbolic film, significantly affecting the dispersion relation and DOS of the hybrid polaritons of

\*yihongliang@hit.edu.cn

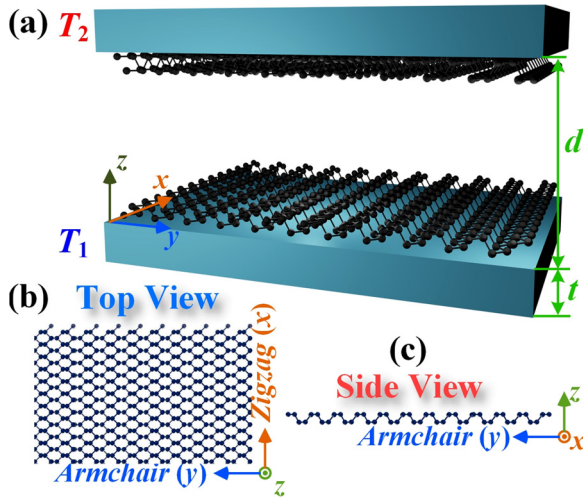


FIG. 1. (a) Schematic of near-field thermal radiation between two aligned heterostructures. Each heterostructure contains *hBN* film covered by monolayer black phosphorus (BP). The thickness of the *hBN* film is denoted as  $t$ . Crystalline structure of the BP from (b) top view and (c) lateral view.

heterostructure [53]. An open question is whether dispersion engineering emerges under the anisotropy-oriented hybridization between hyperbolic waveguide modes and anisotropic SPPs, elevating the photon tunneling and RHF. Thus far, the influence of the strong hybridization between hyperbolic waveguide modes and anisotropic SPPs on NFTR is not well understood.

For these reasons, in this paper, we take a heterostructure composed of lightly doped monolayer BP and hexagonal boron nitride (*hBN*) film as an example and reveal the role of an anisotropic hybrid mode (hyperbolic phonon-elliptic SPPs) in enhancing photon tunneling and NFTR. We theoretically predict that the anisotropy-oriented hybridization in this heterostructure can not only modulate the intensity of photon tunneling but also enable a remarkable topological reconstitution of polaritons. Moreover, we perform the evolutionary

trajectory of such hybrid polariton modes at different film thicknesses and then investigate how this evolution modulates the RHF and photon tunneling.

## II. THEORETICAL ASPECTS

We consider the configuration of NFTR between two aligned heterostructures with temperatures  $T_{1(2)} = 300$  (310) K and vacuum gap  $d$  [Fig. 1(a)]. The heterostructure consists of the 2D material with elliptic SPPs and the *hBN* film. The thickness of the *hBN* film is denoted as  $t$ . The elliptic surface plasmon can be obtained in many material platforms, such as from BP [49], borophene [54], germanium selenide [55],  $T_d$ -WTe<sub>2</sub> [56], and other 2D materials. Since BP can provide robust elliptic surface plasmon in the midinfrared region where Reststrahlen bands of *hBN* appear [57], we consider that BP is an appropriate platform to exhibit the strong hybrid effect between hyperbolic phonon polariton (waveguide) modes and elliptic surface plasmon. The optical properties of *hBN* and BP have also been addressed in the Supplemental Material [58].

As shown in Figs. 1(b) and 1(c), the zigzag and armchair crystalline directions of BP are named  $x$  and  $y$  axes, respectively. The NFTR of this heterostructure can be characterized by the RHF. From the fluctuational electrodynamics, the RHF can be expressed as [66,67]

$$q = \int_0^\infty g(\omega, T_1, T_2) \frac{d\omega}{2\pi} \int_0^{2\pi} \int_0^\infty \xi(\omega, k, \psi) \frac{kd k d\psi}{(2\pi)^2}, \quad (1)$$

where

$$g(\omega, T_1, T_2) = \frac{\hbar\omega}{\exp(\frac{\hbar\omega}{k_B T_2}) - 1} - \frac{\hbar\omega}{\exp(\frac{\hbar\omega}{k_B T_1}) - 1}. \quad (2)$$

Here,  $k$  and  $\psi$  are the wave vector and the azimuthal angle in the  $x$ - $y$  plane, respectively. Additionally, we define the spectral RHF  $q(\omega)$  as the RHF per unit of photonic energy (frequency). The  $\xi(\omega, k, \psi)$  is known as the photon transmission coefficient (PTC), implying the tunneling probability of photon. It can be written as [66]

$$\xi(\omega, k, \psi) = \begin{cases} \text{Tr}[(\mathbf{I} - \mathbf{R}^* \mathbf{R} - \mathbf{T}^* \mathbf{T}) \mathbf{D} (\mathbf{I} - \mathbf{R} \mathbf{R}^* - \mathbf{T} \mathbf{T}^*) \mathbf{D}^*], & k < k_0 \\ \text{Tr}[(\mathbf{R}^* - \mathbf{R}) \mathbf{D} (\mathbf{R} - \mathbf{R}^*) \mathbf{D}^*] \exp(-2|k_{z0}|d), & k > k_0 \end{cases}, \quad (3)$$

where  $k_0 = \omega/c$  and  $k_{z0} = \sqrt{k_0^2 - k^2}$  are the wave vector and the out-of-plane wave vector in vacuum, respectively. When the in-plane wave vector  $k$  is smaller than  $k_0$ , the electromagnetic waves excited by thermal energy are in propagating mode. Otherwise, it is an evanescent wave. Here,  $\mathbf{I}$  is the identity matrix. The usual Fabry-Pérot-like denominator matrix is expressed as  $\mathbf{D} = [\mathbf{I} - \mathbf{R} \mathbf{R} \exp(2ik_{z0}d)]^{-1}$ . In this expression, the reflection coefficient matrix  $\mathbf{R}$  and the transmission coefficient matrix  $\mathbf{T}$  have the following generic forms:

$$\mathbf{R} = \begin{pmatrix} r^{ss} & r^{sp} \\ r^{ps} & r^{pp} \end{pmatrix}, \quad \mathbf{T} = \begin{pmatrix} t^{ss} & t^{sp} \\ t^{ps} & t^{pp} \end{pmatrix}. \quad (4)$$

Here,  $r^{\alpha,\beta}$  and  $t^{\alpha,\beta}$  with  $\alpha, \beta = p, s$  are the reflection and the transmission amplitudes. They can be calculated by the transfer matrix methods, and the detailed derivation is given in the Supplemental Material [58].

## III. RECONSTITUTION AND ENHANCEMENT OF SURFACE STATE IN HETEROSTRUCTURE

To obtain a visual evaluation for the influence of hybrid effect between *hBN* and BP on NFTR, the RHF of three kinds of terminal structure are shown in Fig. 2(a): (I) the individual BP sheet, (II) the individual *hBN* film, and (III) the heterostructure composed of BP sheet and *hBN* film. In

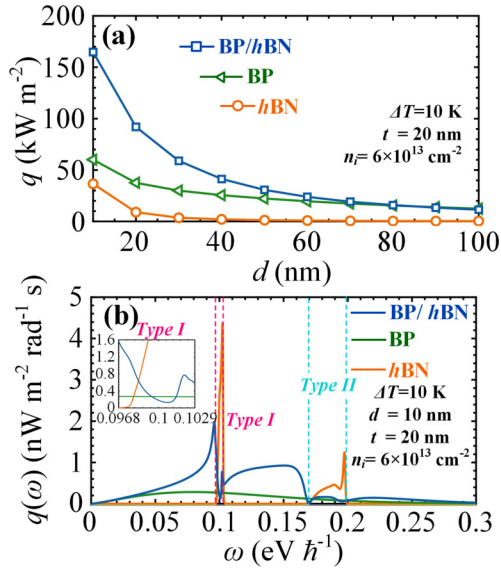


FIG. 2. (a) The radiative heat fluxes (RHF) for three kinds of terminal structures at different vacuum gaps. Three terminal structures are considered: (I) the individual black phosphorus (BP) sheet, (II) the individual  $h\text{BN}$  film, and (III) the heterostructure composed of BP sheet and  $h\text{BN}$  film. (b) Spectral RHF for different terminal structures at  $d = 10 \text{ nm}$ . The thickness of the  $h\text{BN}$  film is fixed at  $20 \text{ nm}$ . The doping density of BP is  $6 \times 10^{13} \text{ cm}^{-2}$ .

this section, the thickness of the  $h\text{BN}$  film is fixed at  $20 \text{ nm}$ . As shown in Fig. 2(a), the RHF of the individual BP sheet and the individual  $h\text{BN}$  film are  $60.05 \text{ kW m}^{-2}$  and  $36.67 \text{ kW m}^{-2}$  for  $d = 10 \text{ nm}$ , respectively. Interestingly, when a monolayer BP is transferred to the surface of the  $h\text{BN}$  film, the RHF of the heterostructure significantly exceeds that of other terminal structures, especially at the small vacuum gap. One can see that the heterostructure can produce  $q = 164.85 \text{ kW m}^{-2}$  for  $d = 10 \text{ nm}$ , which is  $>4.5$  times larger than the RHF of the individual  $h\text{BN}$  film. It is noticed that, however, this enhancement diminishes significantly with the increased gap. This is because the increase in vacuum gap deteriorates the near-field coupling of the hybrid polaritons, resulting in a significant descent of evanescent contribution supported by the hybrid polaritons. As presented in Fig. 2(a), when the vacuum gap increases to  $90 \text{ nm}$ , the RHF of the individual BP begins to outperform that of the heterostructure.

The application of a spectral analysis allows us to understand the mechanism for the enhanced NFTR of the heterostructure. In Fig. 2(b), we show the spectral RHF of three terminal structures at  $d = 10 \text{ nm}$ . One can see that the spectral RHF of the  $h\text{BN}$  film mainly concentrates within the two Reststrahlen bands supported by the hyperbolic waveguide modes. Two peaks contributed by the type-I and II hyperbolic waveguide modes can reach  $4.37$  and  $1.22 \text{ nW m}^{-2} \text{ rad}^{-2} \text{ s}$ , respectively. Figure 2(b) shows that, although the maximum value of spectral RHF is only  $0.28 \text{ nW m}^{-2} \text{ rad}^{-2} \text{ s}$ , the broad resonant frequency range (from  $0$  to  $0.3 \text{ eV } \hbar^{-1}$ ) enables the BP sheet to yield stronger thermal radiation. When the BP sheet is coated on the surface of  $h\text{BN}$ , the spectral RHF of the near-field system undergoes a significant morph, as shown in Fig. 2(b). The heterostructure combines the spectral

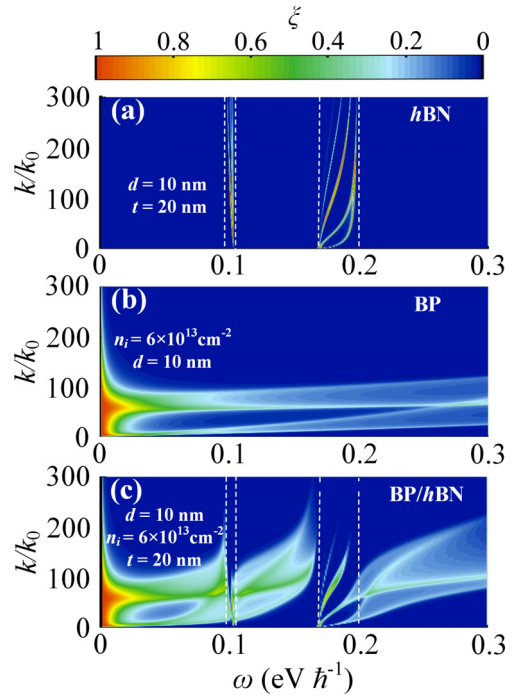


FIG. 3. The photon transmission coefficient of (a) the individual  $h\text{BN}$  film, (b) the individual black phosphorus (BP) sheet, and (c) the heterostructure composed of BP sheet and  $h\text{BN}$  film. The white dashed lines represent the Reststrahlen bands of  $h\text{BN}$  film. The vacuum gap, the thicknesses of  $h\text{BN}$  film, and the doping density of BP are fixed at  $10 \text{ nm}$ ,  $20 \text{ nm}$ , and  $6 \times 10^{13} \text{ cm}^{-2}$ , respectively.

features of  $h\text{BN}$  film and BP. Figure 2(b) shows that the spectral RHF maintains relatively high values both inside and outside the Reststrahlen bands. Compared with the individual BP sheet, the introduction of the  $h\text{BN}$  film improves the spectral characteristic of BP effectively. We take the spectral RHF at  $\omega = 0.959$  and  $0.15 \text{ eV } \hbar^{-1}$  as examples. The spectral RHF at given frequencies increase respectively from  $0.27$  and  $0.16 \text{ nW m}^{-2} \text{ rad}^{-2} \text{ s}$  to  $1.96$  and  $0.92 \text{ nW m}^{-2} \text{ rad}^{-2} \text{ s}$  [Fig. 2(b)]. Additionally, it is worth pointing out that, because of the strong hybridization effect, the spectral RHF of this heterostructure would experience a remarkable nonmonotonic trend in the type-I Reststrahlen band. This also implies that a complex reconfiguration of surface state would occur in this frequency range induced by the strong hybridization effect.

The mechanisms behind the phenomenon of the hybridization effect can be explored by photon tunneling between the two heterostructures (i.e., PTC). To gain a clear evaluation of the hybridization effect, we first briefly review the surface modes of the individual  $h\text{BN}$  film [Fig. 3(a)] and the individual BP sheet [Fig. 3(b)]. The multiple tunneling branches resulting from the hyperbolic phonon waveguide modes of the  $h\text{BN}$  film can be identified in the type-I and II Reststrahlen bands in Fig. 3(a). Its resonance branches can extend to the higher wave vector region  $\sim 300 k_0$  due to the low losses within the  $h\text{BN}$  film. This is the main reason why the  $h\text{BN}$  film can excite higher spectral RHF in the Reststrahlen bands. Additionally, the distribution of the bright branches is in good agreement with Ref. [38], which also shows that our calculations are correct. It is important to emphasize here that

losses in the materials have a significant impact on near-field radiative heat transfer. Let us take the example of the  $h$ BN film. If the losses in  $h$ BN are artificially ignored [that is,  $\text{Im}(\epsilon_{h\text{BN}}) = 0$ ], the material would not absorb the evanescent wave well and cannot induce an obvious near-field effect of radiative heat transfer [68]. The bright branches cover a broad frequency region with a small wave vector in Fig. 3(b) for the BP sheet. This thoroughly explains the spectral feature of the BP sheet shown in Fig. 2(b).

When the monolayer BP is transferred to the surface of the  $h$ BN film, the photon tunneling is significantly enhanced and reconfigured, as Fig. 3(c) shows. The localized fields of surface plasmons of BP outside the hyperbolic Reststrahlen bands are enhanced in the heterostructure due to the interference effect of the  $h$ BN substrate. These intensified polaritons outside the hyperbolic Reststrahlen bands are identified as the elliptical surface plasmon-phonon polariton (ESPPP) mode. Figure 3(c) shows that the wave vector of the ESPPP mode can be effectively increased  $>200 k_0$  at frequencies close to the Reststrahlen bands. This strong photon tunneling may further explain the spectral enhancement outside the Reststrahlen bands shown in Fig. 2(b). The polaritons inside the two Reststrahlen bands of  $h$ BN are hybrid modes between elliptic SPPs and hyperbolic phonon waveguide modes, called the elliptical-hyperbolic surface plasmon-phonon polariton (EHSPPP) mode. The hybrid effect would exhibit a significant difference in the two Reststrahlen bands. From Fig. 3(c), it is evident that the EHSPPP mode in the type-II Reststrahlen band preserves the multiple waveguide mode features like the individual  $h$ BN film, while this feature is not evident for the EHSPPP mode of the type-I Reststrahlen band. Furthermore, the PTCs of the EHSPPP mode in all Reststrahlen bands can still yield a robust bright branch, but its wave vector is compressed observably to a lower region. For the EHSPPP mode of the type-I Reststrahlen band, the wave vector of bright branches is only  $100 k_0$ , as exhibited in Fig. 3(c). It is noticed that the nonlocal effects on the optical properties of materials at the large wave vector region is an important physical phenomenon [69]. As pointed out in Refs. [69–71], for phononic materials (or 2D plasmonic monolayer material), the nonlocal correction to optical properties should be considered when the wave vector is greater than the inverse of the out-of-plane atomic layer spacing  $a$  (or  $\sim 3 \times 10^8$  to  $10 \times 10^8 \text{ m}^{-1}$ ). The nonlocal effects of BP and  $h$ BN are not considered in this paper since the wave vectors we are currently dealing with are smaller than the above wave vector range. However, when the vacuum gap is further reduced, i.e., when the wave vector range of photon tunneling is further increased, the above nonlocal effects may need to be considered.

To understand the influence of anisotropy-oriented hybridization on photon tunneling, Figs. 4–6 show the contour plots of in-plane PTC  $\xi(\omega, k_x, k_y)$  for this heterostructure. Here, we convert  $\xi(\omega, k, \psi)$  to  $\xi(\omega, k_x, k_y)$  utilizing the equations  $k_x = k \cos(\psi)$  and  $k_y = k \sin(\psi)$ . Let us review the PTC features of the BP sheet in Figs. 4(a) and 4(c). At each given frequency, the PTC of the BP sheets clearly shows a bright elliptical band, which matches with the results predicted by the conductivity of BP ( $\text{Im}[\sigma_{xx,yy}] > 0$ ). Additionally, because of the coupling between the evanescent fields of the top and bottom vacuum/BP interfaces, the surface state would

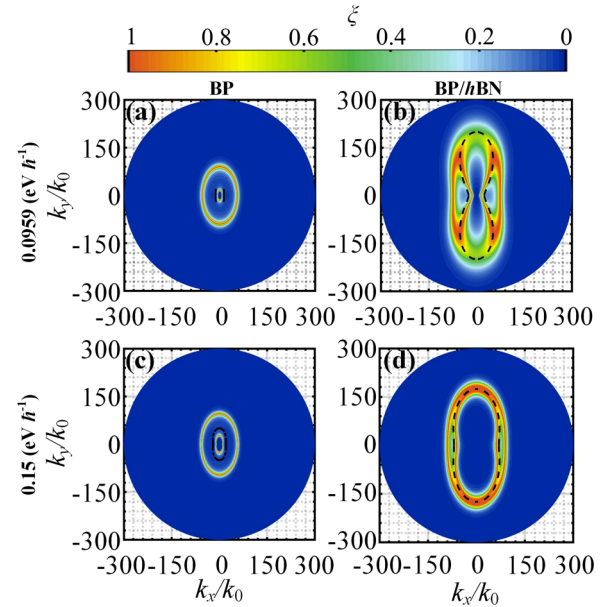


FIG. 4. In-plane photon transmission coefficient (PTC) of (a) the black phosphorus (BP) sheet and (b) the heterostructure for the frequency of  $0.0959 \text{ eV } \hbar^{-1}$ . In-plane PTC of (c) the BP sheet and (d) the heterostructure for the frequency of  $0.15 \text{ eV } \hbar^{-1}$ . These dashed curves represent the isofrequency dispersion given in each panel.

split into two resonant branches, i.e., the antisymmetric and symmetric mode, as shown in Figs. 4(a) and 4(c). To confirm the dominant role of elliptical SPPs in the photon tunneling of BP, we exhibit the in-plane isofrequency dispersion at each given frequency in Figs. 4(a) and 4(c). It is shown that all dashed lines are elliptical and unambiguously located between the symmetric and antisymmetric branches. When the monolayer BP is transferred to the surface of the  $h$ BN film, it is first noticed that the bright branches supported by the ESPPP mode of the heterostructure still show a closed topology (ellipse), as exhibited in Figs. 4(b) and 4(d). The in-plane isofrequency dispersions of the ESPPP mode of the heterostructure under all frequencies also remain elliptical, matching well with the bright branches of the PTCs. This

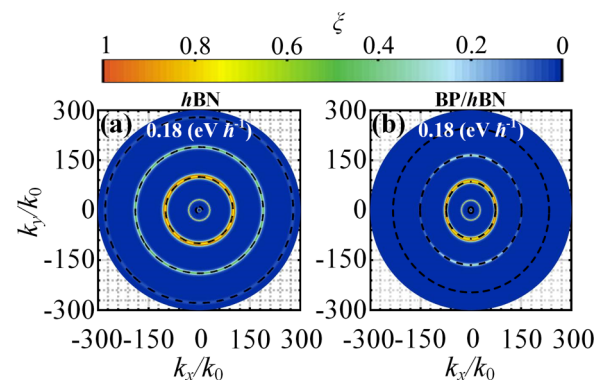


FIG. 5. In-plane photon transmission coefficient (PTC) of (a) the  $h$ BN film and (b) the heterostructure at  $\omega = 0.18 \text{ eV } \hbar^{-1}$ . These dashed curves represent the isofrequency dispersion given in each panel.

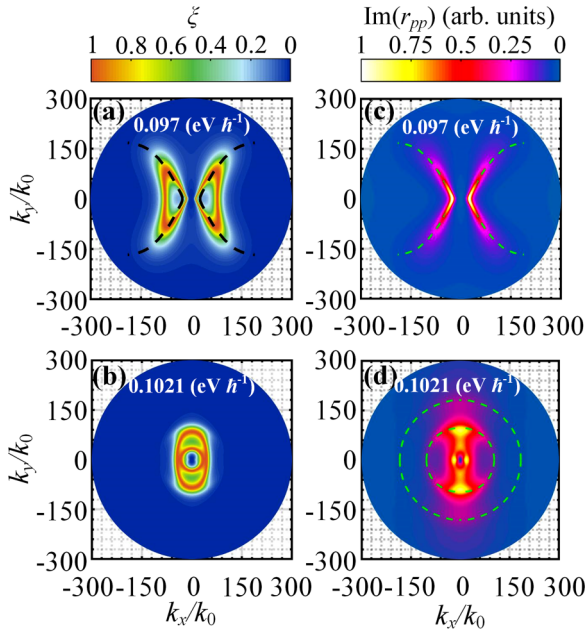


FIG. 6. In-plane photon transmission coefficient (PTC) of the heterostructure at a frequency of (a)  $0.097 \text{ eV } \hbar^{-1}$  and (b)  $0.1021 \text{ eV } \hbar^{-1}$ . Imaginary part of the reflection coefficients  $\text{Im}(r_{pp})$  of the heterostructure for (c)  $\omega = 0.097 \text{ eV } \hbar^{-1}$  and (d)  $\omega = 0.1021 \text{ eV } \hbar^{-1}$ . These dashed curves are the isofrequency dispersion given in each panel.

can be explained by the fact that the ESPPP mode of the heterostructure is still dominated by BP at these frequencies since the  $h\text{BN}$  film cannot provide a robust evanescent field outside the two Reststrahlen bands. Anisotropy-oriented hybridization between BP and the  $h\text{BN}$  film cannot transform the intrinsic topological structure of BP outside the two Reststrahlen bands. However, the symmetrical and antisymmetric resonance branches form a continuous region [Figs. 4(b) and 4(d)] since the hybrid effect in the heterostructure destroys the coupling between the evanescent fields of the top and bottom BP interfaces. Additionally, compared with the elliptical SPPs of BP, the ESSSP mode of the heterostructure can provide a stronger surface state at the same frequency, improving the photon tunneling of the system effectively. Figure 4 shows that the bright branches not only become more robust but also move toward a larger wave vector region. One can see that, for  $\omega = 0.15 \text{ eV } \hbar^{-1}$ , the wave vector of the ESSSP mode can reach  $240 k_0$ , which is  $>2$  times that of the elliptical SPPs of the BP.

The phenomenon of anisotropy-oriented hybridization in the two Reststrahlen bands is elaborated in the following. As a natural hyperbolic material, the  $h\text{BN}$  film can support hyperbolic phonon waveguide modes in two Reststrahlen bands: (i) type-I spectral regions ( $0.0967\text{--}0.1029 \text{ eV } \hbar^{-1}$ ) with negative out-of-plane permittivity ( $\epsilon_{\perp} < 0$ ) and positive in-plane permittivity ( $\epsilon_{\parallel} > 0$ ); (ii) type-II spectral regions ( $0.1699\text{--}0.1996 \text{ eV } \hbar^{-1}$ ) with positive out-of-plane permittivity ( $\epsilon_{\perp} > 0$ ) and negative in-plane permittivity ( $\epsilon_{\parallel} < 0$ ). Let us review the PTC characteristics of the  $h\text{BN}$  film in Fig. 5(a). From the plot, it becomes apparent that multiple bright branches exist due to the Fabry-Pérot effect of hyper-

bolic waveguide modes in the  $h\text{BN}$  film. Figure 5(b) illustrates the PTC of the EHSPPP mode supported by the heterostructure in the type-II Reststrahlen band ( $\omega = 0.18 \text{ eV } \hbar^{-1}$ ). Here, one can see that the EHSPPP mode in the type-II Reststrahlen band preserves the multiple resonance feature, which supports multiple bright branches. It is worth pointing out that, for the type-II Reststrahlen band, the bright branches of the EHSPPP mode in the heterostructure are approximated by an ellipse [Fig. 5(b)] as opposed to the in-plane isotropy in the  $h\text{BN}$  film [Fig. 5(a)]. Additionally, to clearly identify the in-plane isotropy of the EHSPPP mode, Fig. 5(b) shows the isofrequency dispersion lines for the heterostructure. One can see that these black dashed lines are nicely located at the bright branches, which unambiguously demonstrates the anisotropic multiple resonance features of the EHSPPP mode. This phenomenon can be understood as follows: BP has highly anisotropic constraints on the evanescent field, which allows a stronger anisotropic hybridization with the hyperbolic waveguide modes of the  $h\text{BN}$  film and results in a higher difference in phonon waveguide propagation along the different directions. Since the greater electromagnetic loss along the zigzag crystal axis of BP slows down the wave propagation, the resonance of the EHSPPP mode at this direction is thus limited to a smaller wave vector region, as exhibited in Fig. 5(b). However, this hybrid effect does not improve the photon tunneling of such a heterostructure in type-II Reststrahlen bands. Figure 5(a) shows that the bright resonance branches of hyperbolic waveguide modes in the  $h\text{BN}$  film can be inspired when  $k$  is  $\sim 220 k_0$ . By comparison, Fig. 5(b) indicates that the anisotropy-oriented hybridization induces an early truncation of the EHSPPP mode, and the bright resonance branches disappear at  $\sim 150 k_0$ . This early truncation also explains well why, in the type-II Reststrahlen bands, the heterostructure has a lower spectral RHF than the  $h\text{BN}$  films, as indicated in Fig. 2(b).

Interestingly, we find that the anisotropy-oriented hybridization in this heterostructure would induce dispersion engineering in the type-I Reststrahlen band. Figures 6(a) and 6(b) illustrate the contour of PTCs of the EHSPPP mode at the frequencies of  $0.097$  and  $0.1021 \text{ eV } \hbar^{-1}$ , respectively. By means of the above analysis, the intrinsic topologies of both BP and  $h\text{BN}$  are closed. Nevertheless, as shown in Fig. 6(a), it can be clearly seen that the bright branches of the polaritons in this heterostructure create an open topological structure (quasihyperbolic structure) at  $\omega = 0.097 \text{ eV } \hbar^{-1}$ . This is caused by the anticrossing hybridization effect between elliptical SPPs in BP and type-I hyperbolic waveguide modes in the  $h\text{BN}$  film. Unlike the polaritons in the graphene/ $h\text{BN}$  heterostructure, where similar fringe patterns can be supported because of in-plane isotropic nature, the anisotropy-oriented hybridization would maximize the in-plane anisotropy, leading to a topological transition of polaritons. Similarly, in the imaginary part of the  $p$ -polarized reflection coefficients, there are bright hyperbolic branches, matching with the results calculated by the PTC of the EHSPPP mode. Note that, since the  $p$ -polarized evanescent field is the main contribution to the NFTR of BP and  $h\text{BN}$  [38,49–51], we only present the  $p$ -polarized reflection coefficients here. However, this hyperbolic property is unstable and ephemeral. As the frequency increases to  $0.1021 \text{ eV } \hbar^{-1}$ , the topology of the EHSPPP mode

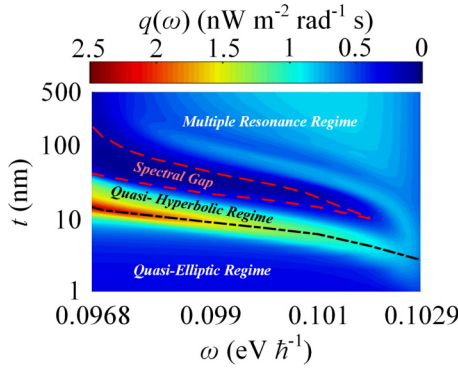


FIG. 7. Spectral radiative heat fluxes (RHF) for different thicknesses of  $h$ BN film inside the type-I hyperbolic Reststrahlen band. The vacuum gap is 10 nm. The thickness of  $h$ BN film is restricted in the range of  $t \in [1, 500]$  nm.

would resume to a closed structure in Figs. 6(b) and 6(d). The conductivity of BP and the permittivity of  $h$ BN change with the increasing of frequency, so there are many independent variables at different frequencies, which seriously interferes with qualitative analysis of why the EHSPPP mode resumes to closed topology with increasing frequency. Thus, in the subsequent section, we will adopt the thickness of the  $h$ BN film as a single variable to elaborate in detail on the evolution of the EHSPPP mode and its topological transition processes.

#### IV. EFFECT OF $h$ BN FILM THICKNESS ON THE HYBRID POLARITONS MODE

It is worth mentioning that film thickness can strongly affect the hyperbolic phonon waveguide modes of the  $h$ BN film [72–74], resulting in a notable modification of anisotropy-oriented hybridization in the heterostructure. In this section, we turn now to discuss how the thickness of  $h$ BN films affects the thermal radiation and photon tunneling in this heterostructure. In view of the discussion above, because of the anisotropy-oriented hybridization, the EHSPPP mode exhibits different features in contrast to the elliptical SPPs of BP and the hyperbolic waveguide modes of  $h$ BN, and it may contain even richer dispersion phenomena. We first investigate the thickness effect on the spectral feature of the heterostructure inside the type-I hyperbolic Reststrahlen band. It is first noticed that the spectral RHF is insensitive to the variation of thickness when  $t$  is large ( $>400$  nm). Thus, the thickness of the  $h$ BN film of Fig. 7 is restricted in the range of  $t \in [1, 500]$  nm. In Fig. 7, we show the thickness effect on spectral RHF of the EHSPPP mode inside the type-I hyperbolic Reststrahlen band. There are three salient features: (i) As the thickness increases, the spectral RHF would go through three regimes, namely, the quasi-elliptic, quasi-hyperbolic, and multiple resonance regimes. (ii) The increase of thickness enables spectral RHF to show an increase-decrease-increase trend, in which spectral RHF would exhibit a spectral gap. (iii) The maximum value of the spectral RHF occurs when the EHSPPP mode changes from the quasi-elliptic form to the quasi-hyperbolic form.

Next, to better understand the mechanism of the above spectral results, we show the in-plane PTC and isofrequency

dispersion with thicknesses of 1, 10, 12, 15, 25, 50, 100, and 200 nm, respectively, in Figs. 8(a)–8(h). The frequency is fixed at  $0.098 \text{ eV } \hbar^{-1}$ . As one can see, the evolutionary trajectory of the EHSPPP mode at different  $h$ BN film thicknesses can be clearly presented. When the thickness of the  $h$ BN film is fixed at 1 nm, we notice that the resonance branches of the EHSPPP mode exhibit elliptic topology. This phenomenon can be understood by the approximate dispersion relation of the independent  $h$ BN film, which can be expressed as [72]

$$k_l = \frac{\psi}{k_{0t}} \left[ 2 \arctan \left( \frac{i}{\sqrt{\varepsilon_{\perp} \varepsilon_{\parallel}}} \right) + \pi l \right], \quad l = 0, 1, \dots, \quad (5)$$

where  $k_l$  is the in-plane wave vector of dispersion of the  $h$ BN film, and  $\psi = i\sqrt{\varepsilon_{\perp}/\varepsilon_{\parallel}}$ . According to the approximate dispersion relation, it can be derived that hyperbolic waveguide modes of the  $h$ BN film are located at an ultrahigh wave vector regime (much larger than the wave vector of elliptic SPPs in BP), when the thickness of the  $h$ BN film is 1 nm. Thus, for the case with  $t = 1$  nm, the EHSPPP mode is governed by the evanescent field of BP, exhibiting the bright elliptic branches, as Fig. 8(a) shows. As the thickness increases to 9 nm, the dispersion of the  $h$ BN film shrinks drastically to a smaller wave vector region, where the dispersion feature can be predicted by Eq. (5), greatly invigorating the anisotropy-oriented polariton hybridization in the heterostructure. Moreover, the increase in thickness expands the elliptic dispersion curve governed by BP to a higher wave vector range. For the sake of subsequent discussion, we define this dispersion as a one-order dispersion of the EHSPPP mode. Figure 8(b) shows that a significant dispersion variation appears for the minimum-order hyperbolic phonon waveguide mode due to the anisotropy-oriented hybridization. We note that this dispersion differs significantly from the circular guided mode of the  $h$ BN film. It exhibits a figure-eight-like topology and can be excited along the  $y$  axis only for the lower wave vectors. We define this dispersion as a two-order dispersion of the EHSPPP mode. As the thickness further increases, the above dispersion change would be more pronounced, with the one- and two-order dispersion lines closer to each other along the  $y$  axis. When the thickness is 12 nm, the EHSPPP mode of the heterostructure would be reconstituted topologically, exhibiting quasihyperbolic-like bright branches. One can see that the black dashed lines are nicely located at the bright branches, which unambiguously demonstrates the quasihyperbolic-like features of the EHSPPP mode.

The observed topological transition can be explained as follows: when two dispersions are infinitely close to each other, the anticrossing hybridization effect occurs since two in-plane dispersions cannot overlap, resulting in an opening topology (quasihyperbolic shape) of the EHSPPP mode. This similar anticrossing effect was also found in the moiré hyperbolic metasurfaces [75–77], the graphene/ $h$ BN heterostructure [38–40,78], and the graphene/SiC heterostructure [79,80]. Additionally, this topological transition can extend effectively the wave vector region occupied by the EHSPPP mode, improving the photon tunneling of the heterostructure. This also explains why the maximum spectral RHF occurs when the EHSPPP mode changes from the quasi-elliptic form to the quasihyperbolic form in Fig. 7. However, due to the

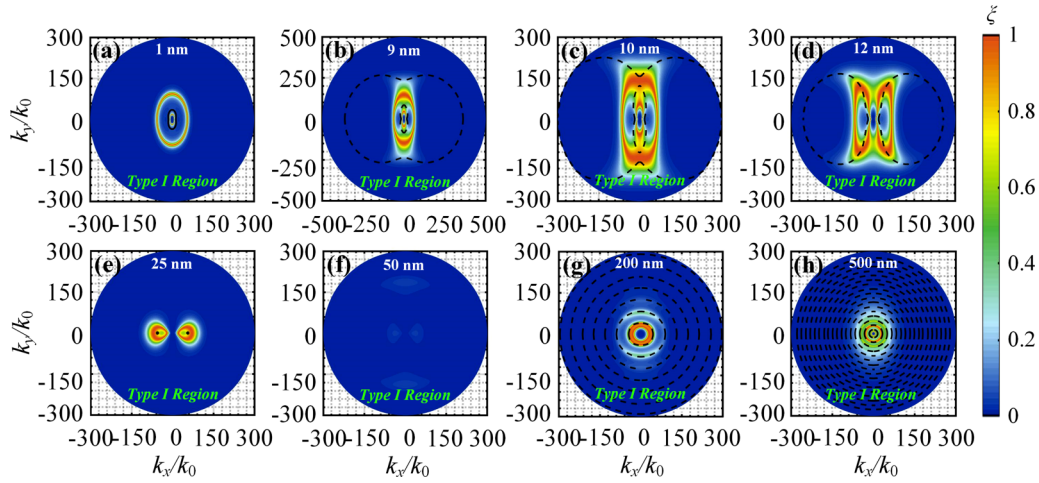


FIG. 8. In-plane photon transmission coefficient (PTC) of the heterostructure at the frequency of  $0.098 \text{ eV } \hbar^{-1}$  for (a)  $t = 1 \text{ nm}$ , (b)  $t = 9 \text{ nm}$ , (c)  $t = 10 \text{ nm}$ , (d)  $t = 12 \text{ nm}$ , (e)  $t = 25 \text{ nm}$ , (f)  $t = 50 \text{ nm}$ , (g)  $t = 200 \text{ nm}$ , and (h)  $t = 500 \text{ nm}$ . These dashed curves represent the isofrequency dispersion given in each panel.

mode repulsion from higher-order phonon waveguide modes of the  $h\text{BN}$  film, the increased  $t$  in Fig. 8(e) leads to the decrease in the wave vector range of quasihyperbolic branches. For the case with  $t = 50 \text{ nm}$ , it is difficult to observe the quasihyperbolic bright branches due to this mode repulsion [Fig. 8(f)], corresponding to the spectral gap of Fig. 7. When the thickness is fixed at  $200 \text{ nm}$ , the results show that there exists a strong multiple tunneling resonance in the contour of the in-plane PTC. However, one can see that the isofrequency dispersion of this multiple tunneling resonance is still weakly anisotropic, unlike the multiple waveguide modes of pure  $h\text{BN}$  film with in-plane isotropy. Let us take the innermost dispersion as an example in Fig. 8(g). Its wave vectors along the  $y$  and  $x$  axes are  $40 k_0$  and  $45 k_0$ , respectively, exhibiting weak anisotropy. As the thickness increases to  $500 \text{ nm}$ , Fig. 8(h) shows that this multiple tunneling resonance becomes more pronounced, enhancing the photon tunneling of the heterostructure. This result also explains the enhancement effect of increasing thickness on the spectral RHF inside the multiple resonance regime of Fig. 7. Meanwhile, for  $t = 500 \text{ nm}$ , the dispersion of the EHSPPP mode is also anisotropic. The wave vectors of the innermost dispersion line along the  $y$  and  $x$  axes are  $15 k_0$  and  $16 k_0$ , respectively.

As discussed above, the EHSPPP modes of the type-I and II Reststrahlen bands would show very different hybrid effects due to the different hyperbolic features of  $h\text{BN}$  in the two Reststrahlen bands. We focus here on the calculation of the spectral RHF inside type-II Reststrahlen bands of the  $h\text{BN}$  film at different thicknesses [see Fig. 9]. Here, we define the spectral contour inside type-II Reststrahlen bands as the quasi-elliptic regime with low spectral RHF and the multiple resonance regime with high spectral RHF. Let us take the case with  $\omega = 0.18 \text{ eV } \hbar^{-1}$  as an example. When the thickness is  $< 8 \text{ nm}$ , the variation of thickness does not substantially improve the spectral RHF. Within this range of  $t \in [1, 8] \text{ nm}$ , the spectral RHF of the system is always  $< 0.08 \text{ nW m}^{-2} \text{ rad}^{-2} \text{ s}$ . It is first noticed that, when the thickness is increased beyond  $8 \text{ nm}$ , there is a dramatic increase in spectral RHF, achieving  $0.22 \text{ nW m}^{-2} \text{ rad}^{-2} \text{ s}$  at  $t = 500 \text{ nm}$ .

Finally, we analyze the thickness effect of the BP/ $h\text{BN}$  heterostructure inside the type-II Reststrahlen band. In Fig. 10, the in-plane PTC and isofrequency dispersion are plotted for different thicknesses at  $\omega = 0.18 \text{ eV } \hbar^{-1}$ . For  $t = 1 \text{ nm}$ , the hybrid effect in the heterostructure is weak, and the EHSPPP mode is governed by the evanescent field of BP, like the case inside the type-I Reststrahlen band [Fig. 10(a)]. In Figs. 10(b)–10(d), more orders of bright branches appear with the increase in thickness and eventually merge to a continuous band when the  $h\text{BN}$  film is increased to  $500 \text{ nm}$ . This also explains why the thicker film is effective in improving the spectral RHF of this heterostructure in Fig. 9. Additionally, it is noticed that the resonance branches inside the type-II Reststrahlen band exhibit elliptical fringes under all thicknesses [Fig. 10], in which the optical axis of elliptical fringes is parallel to that of BP. This can be explained by the fact that the BP sheet is analogous to a converter, leading to anisotropic propagation with the elliptical fringes of the waveguide mode for the  $h\text{BN}$  film.

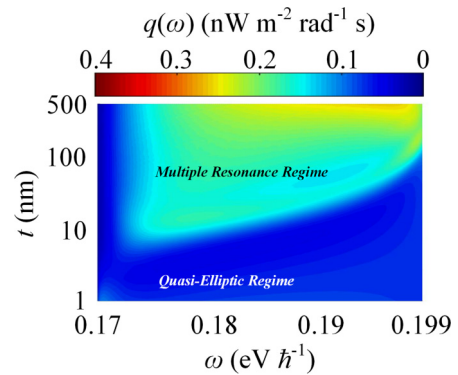


FIG. 9. Spectral radiative heat fluxes (RHF) for different thicknesses of  $h\text{BN}$  film inside the type-II hyperbolic Reststrahlen band. The vacuum gap is  $10 \text{ nm}$ . The thickness of  $h\text{BN}$  film is restricted in the range of  $t \in [1, 500] \text{ nm}$ .

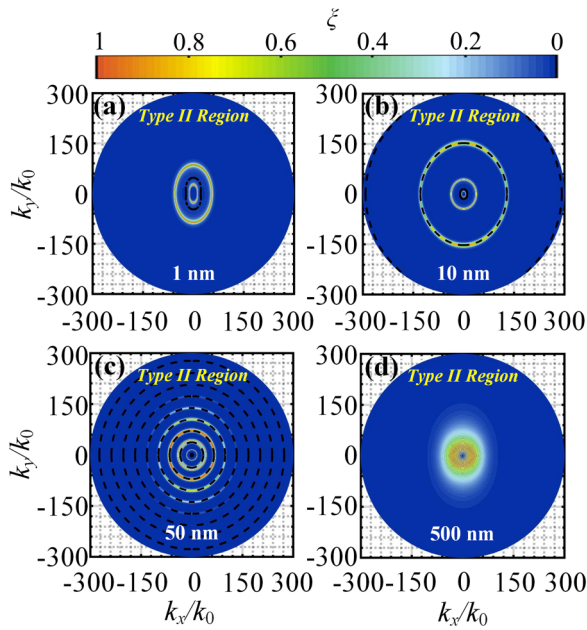


FIG. 10. In-plane photon transmission coefficients (PTCs) of the heterostructure at the frequencies of  $0.18 \text{ eV } \hbar^{-1}$  for (a)  $t = 1 \text{ nm}$ , (b)  $t = 10 \text{ nm}$ , (c)  $t = 50 \text{ nm}$ , and (d)  $t = 500 \text{ nm}$ . These dashed curves represent the isofrequency dispersion given in each panel.

## V. CONCLUSIONS

The application of hybrid modes among different polaritons has emerged as a promising way to modulate and improve NFTR. Motivated by the current interest in the enhancement of NFTR, we have presented in this paper a theoretical study of the anisotropic hybrid effect on the radiative heat transfer between two heterostructures composed of a *h*BN film and BP. This heterostructured optical material can enhance photon tunneling and surpasses respectively the individual *h*BN film and BP by a factor of 4.5 and 2.7 times in terms of achieving

high NFTR, thanks to the anisotropic hybridization effect. Moreover, we found that the elliptic SPP of BP can couple with the hyperbolic waveguide modes of the *h*BN film to form an anisotropic hybrid polariton mode, giving rise to a remarkable topological reconstitution for the polariton mode of the heterostructure. Particularly, in the type-I Reststrahlen band of *h*BN, these anisotropic hybrid polaritons enable a topological transition of the surface state from elliptical (closed) to quasi-hyperbolic (open). We explain that this transition is due to the in-plane anticrossing hybridization effect. Lastly, we have systematically exhibited the evolutionary trajectory of this anisotropic hybrid polariton mode as a function of different *h*BN film thicknesses and then investigated how this evolution efficiently modulates the RHF and photon tunneling.

Inducing the anisotropic hybrid polariton mode upon the application of the elliptic SPP and the hyperbolic phonon waveguide modes, as demonstrated in this paper, may also have important consequences for the enhancement and modulation of near-field radiative energy transport. The phenomena identified in this paper can be effectively extended to heterostructures prepared from other 2D materials with elliptical plasmon nature (such as borophene and carbon phosphide) and other hyperbolic films (such as  $\text{Bi}_2\text{Se}_3$  and calcite) and open exotic avenues for the development of more efficient and powerful thermal management and photonic energy harvesting techniques.

## ACKNOWLEDGMENT

This paper was supported by the National Natural Science Foundation of China (Grant No. 52076056), the Fundamental Research Funds for the Central Universities (Grant No. FRFCU5710094020), the Croatian Science Foundation (Grant No. UIP-2019-04-6869), and the European Regional Development Fund for the “Center of Excellence for Advanced Materials and Sensing Devices” (Grant No. KK.01.1.1.01.0001).

- [1] A. Soufiani and J. Taine, High temperature gas radiative property parameters of statistical narrow-band model for  $\text{H}_2\text{O}$ ,  $\text{CO}_2$  and  $\text{CO}$ , and correlated-K model for  $\text{H}_2\text{O}$  and  $\text{CO}_2$ , *Int. J. Heat Mass Transfer* **40**, 987 (1997).
- [2] M. D. Kelzenbergx, S. W. Boettcher, J. A. Petykiewicz, D. B. Turner-Evans, M. C. Putnam, E. L. Warren, J. M. Spurgeon, R. M. Briggs, N. S. Lewis, and H. A. Atwater, Enhanced absorption and carrier collection in Si wire arrays for photovoltaic applications, *Nat. Mater.* **9**, 239 (2010).
- [3] D. Polder and M. Van Hove, Theory of radiative heat transfer between closely spaced bodies, *Phys. Rev. B* **4**, 3303 (1971).
- [4] K. Joulain, J. P. Mulet, F. Marquier, R. Carminati, and J. J. Greffet, Surface electromagnetic waves thermally excited: Radiative heat transfer, coherence properties and Casimir forces revisited in the near field, *Surf. Sci. Rep.* **57**, 59 (2005).
- [5] J. C. Cuevas and F. J. Garcia-Vidal, Radiative heat transfer, *ACS. Photonics* **5**, 3896 (2018).
- [6] Z. M. Zhang, *Nano/Microscale Heat Transfer* (Springer Nature Switzerland AG, Cham, 2020).
- [7] S. A. Biehs, R. Messina, P. S. Venkataram, A. W. Rodriguez, J. C. Cuevas, and P. Ben-Abdallah, Near-field radiative heat transfer in many-body systems, *Rew. Mod. Phys.* **93**, 025009 (2021).
- [8] C. R. Otey, W. T. Lau, and S. Fan, Thermal Rectification through Vacuum, *Phys. Rev. Lett.* **104**, 154301 (2010).
- [9] P. Ben-Abdallah and S. A. Biehs, Near-Field Thermal Transistor, *Phys. Rev. Lett.* **112**, 044301 (2014).
- [10] A. Fiorino, D. Thompson, L. X. Zhu, R. Mittapally, S. A. Biehs, O. Bezencenet, N. El-Bondry, S. Bansropun, P. Ben-Abdallah, E. Meyhofer *et al.*, A thermal diode based on nanoscale thermal radiation, *ACS. Nano* **12**, 5774 (2018).
- [11] J. Ordóñez-Miranda, Y. Ezzahri, J. A. Tiburcio-Moreno, K. Joulain, and J. Drevillon, Radiative Thermal Memristor, *Phys. Rev. Lett.* **123**, 025901 (2019).
- [12] C. Guo, B. Zhao, D. H. Huang, and S. H. Fan, Radiative thermal router based on tunable magnetic Weyl semimetals, *ACS. Photonics* **7**, 3257 (2020).
- [13] A. Narayanaswamy and G. Chen, Surface modes for near field thermophotovoltaics, *Appl. Phys. Lett.* **82**, 3544 (2003).
- [14] A. Fiorino, L. X. Zhu, D. Thompson, R. Mittapally, P. Reddy, and E. Meyhofer, Nanogap near-field thermophotovoltaics, *Nat. Nanotechnol.* **13**, 806 (2018).

- [15] C. Lucchesi, D. Cakiroglu, J. P. Perez, T. Taliercio, E. Tournie, P. O. Chapuis, and R. Vaillon, Near-field thermophotovoltaic conversion with high electrical power density and cell efficiency above 14%, *Nano. Lett.* **21**, 4524 (2021).
- [16] B. Zhao, S. Assaworranit, P. Santhanam, M. Orenstein, and S. H. Fan, High-performance photonic transformers for DC voltage conversion, *Nat. Commun.* **12**, 4684 (2021).
- [17] K. F. Chen, P. Santhanam, S. Sandhu, L. X. Zhu, and S. H. Fan, Heat-flux control and solid-state cooling by regulating chemical potential of photons in near-field electromagnetic heat transfer, *Phys. Rev. B* **91**, 134301 (2015).
- [18] C. W. Lin, B. N. Wang, K. H. Teo, and Z. M. Zhang, A coherent description of thermal radiative devices and its application on the near-field negative electroluminescent cooling, *Energy* **147**, 177 (2018).
- [19] L. X. Zhu, A. Fiorino, D. Thompson, R. Mittapally, E. Meyhofer, and P. Reddy, Near-field photonic cooling through control of the chemical potential of photons, *Nature (London)* **566**, 239 (2019).
- [20] S. Shen, A. Narayanaswamy, and G. Chen, Surface phonon polaritons mediated energy transfer between nanoscale gaps, *Nano. Lett.* **9**, 2909 (2009).
- [21] M. Francoeur, M. P. Mengüç, and R. Vaillon, Spectral tuning of near-field radiative heat flux between two thin silicon carbide films, *J. Phys. D: Appl. Phys.* **43**, 075501 (2010).
- [22] B. Song, Y. Ganjeh, S. Sadat, D. Thompson, A. Fiorino, V. Fernández-Hurtado, J. Feist, F. J. Garcia-Vidal, J. C. Cuevas, P. Reddy *et al.*, Enhancement of near-field radiative heat transfer using polar dielectric thin films, *Nat. Nanotechnol.* **10**, 253 (2015).
- [23] M. Ghashami, H. Geng, T. Kim, N. Iacopino, S. K. Cho, and K. Park, Precision Measurement of Phonon-Polaritonic Near-Field Energy Transfer between Macroscale Planar Structures Under Large Thermal Gradients, *Phys. Rev. Lett.* **120**, 175901 (2018).
- [24] V. Hatamipour, S. Edalatpour, and M. Francoeur, Apparent Spectral Shift of Thermally Generated Surface Phonon-Polariton Resonance Mediated by a Nonresonant Film, *Phys. Rev. Applied* **10**, 054047 (2018).
- [25] P. O. Chapuis, S. Volz, C. Henke, K. Joulain, and J. J. Greffet, Effects of spatial dispersion in near-field radiative heat transfer between two parallel metallic surfaces, *Phys. Rev. B* **77**, 035431 (2008).
- [26] E. Rousseau, M. Laroche, and J. J. Greffet, Radiative heat transfer at nanoscale mediated by surface plasmons for highly doped silicon, *Appl. Phys. Lett.* **95**, 231913 (2009).
- [27] T. Kralik, P. Hanzelka, M. Zobac, V. Musilova, T. Fort, and M. Horak, Strong Near-Field Enhancement of Radiative Heat Transfer between Metallic Surfaces, *Phys. Rev. Lett.* **109**, 224302 (2012).
- [28] L. Tang, J. DeSutter, and M. Francoeur, Near-field radiative heat transfer between dissimilar materials mediated by coupled surface phonon- and plasmon-polaritons, *ACS. Photonics* **7**, 1304 (2018).
- [29] M. Lim, J. Song, S. S. Lee, J. Lee, and B. J. Lee, Surface-Plasmon-Enhanced Near-Field Radiative Heat Transfer between Planar Surfaces with a Thin-Film Plasmonic Coupler, *Phys. Rev. Applied* **14**, 014070 (2020).
- [30] M. Lim, S. S. Lee, and B. J. Lee, Near-field thermal radiation between graphene-covered doped silicon plates, *Opt. Express* **21**, 22173 (2013).
- [31] S. Basu, Y. Yang, and L. P. Wang, Near-field radiative heat transfer between metamaterials coated with silicon carbide thin films, *Appl. Phys. Lett.* **106**, 033106 (2015).
- [32] R. Messina, P. Ben-Abdallah, B. Guizal, and M. Antezza, Graphene-based amplification and tuning of near-field radiative heat transfer between dissimilar polar materials, *Phys. Rev. B* **96**, 045402 (2017).
- [33] H. Iizuka and S. H. Fan, Significant Enhancement of Near-Field Electromagnetic Heat Transfer in a Multilayer Structure Through Multiple Surface-States Coupling, *Phys. Rev. Lett.* **120**, 063901 (2018).
- [34] Z. H. Zheng, A. Wang, and Y. M. Xuan, Spectral tuning of near-field radiative heat transfer by graphene-covered metasurfaces, *J. Quant. Spectrosc. Radiat. Transfer* **208**, 86 (2018).
- [35] K. Z. Shi, Y. C. Sun, Z. Y. Chen, N. He, F. L. Bao, J. Evans, and S. L. He, Colossal enhancement of near-field thermal radiation across hundreds of nanometers between millimeter-scale plates through surface plasmon and phonon polaritons coupling, *Nano. Lett.* **19**, 8082 (2019).
- [36] J. E. Pérez-Rodríguez, G. Pirruccio, and Raúl Esquivel-Sirvent, Spectral gaps in the near-field heat flux, *Phys. Rev. Materials* **3**, 015201 (2019).
- [37] K. Z. Shi, Z. Y. Chen, X. N. Xu, J. L. Evans, and S. L. He, Optimized colossal near-field thermal radiation enabled by manipulating coupled plasmon polariton geometry, *Adv. Mater.* **33**, 2106097 (2021).
- [38] B. Zhao and Z. M. Zhang, Enhanced photon tunneling by surface plasmon-phonon polaritons in graphene/hBN heterostructures, *J. Heat Transfer* **139**, 022701 (2017).
- [39] K. Z. Shi, F. L. Bao, and S. L. He, Enhanced near-field thermal radiation based on multilayer graphene-hBN heterostructures, *ACS. Photonics* **4**, 971 (2017).
- [40] B. Zhao, B. Guizal, and Z. M. Zhang, Near-field heat transfer between graphene/hBN multilayers, *Phys. Rev. B* **95**, 245437 (2017).
- [41] W. B. Zhang, C. Y. Zhao, and B. X. Wang, Enhancing near-field heat transfer between composite structures through strongly coupled surface modes, *Phys. Rev. B* **100**, 075425 (2019).
- [42] R. Q. Wang, J. C. Lu, and J. H. Jiang, Enhancing Thermophotovoltaic Performance Using Graphene-BN-InSb Near-Field Heterostructures, *Phys. Rev. Applied* **12**, 044038 (2019).
- [43] S. McSherry and A. Lenert, Extending the Thermal Near Field Through Compensation in Hyperbolic Waveguides, *Phys. Rev. Applied* **14**, 014074 (2020).
- [44] J. H. Zhang, B. Wang, C. Y. Li, and X. Y. Li, Tunable near-field thermal radiation between graphene-assisted Bi<sub>2</sub>Se<sub>3</sub>, *Case Stud. Therm. Eng.* **28**, 101381 (2021).
- [45] B. Yang, D. Pan, X. D. Guo, H. Hu, and Q. Dai, Substrate effects on the near-field radiative heat transfer between bi-planar graphene/hBN heterostructures, *Int. J. Therm. Sci.* **176**, 107493 (2022).
- [46] O. Ilic, M. Jablan, J. D. Joannopoulos, I. Celanovic, H. Buljan, and M. Soljačić, Near-field thermal radiation transfer controlled by plasmons in graphene, *Phys. Rev. B* **85**, 155422 (2012).
- [47] X. L. Liu and Z. M. Zhang, Giant enhancement of nanoscale thermal radiation based on hyperbolic graphene plasmons, *Appl. Phys. Lett.* **107**, 143114 (2015).
- [48] M. J. He, H. Qi, Y. T. Ren, Y. J. Zhao, and M. Antezza, Active control of near-field radiative heat transfer by graphene-gratings coating-twisting method, *Opt. Lett.* **45**, 2914 (2020).

- [49] J. D. Shen, S. Guo, X. L. Liu, B. Liu, W. T. Wu, and H. He, Super-Planckian thermal radiation enabled by coupled quasi-elliptic 2D black phosphorus plasmons, *Appl. Therm. Eng.* **144**, 403 (2018).
- [50] X. L. Liu, J. D. Shen, and Y. M. Xuan, Near-field thermal radiation of nanopatterned black phosphorene mediated by topological transitions of phosphorene plasmons, *Nanosc. Microsc. Therm.* **23**, 188 (2019).
- [51] H. Hajian, I. D. Rukhlenko, V. Ercaglar, G. Hanson, and E. Ozbay, Epsilon-near-zero enhancement of near-field radiative heat transfer in BP/*h*BN and BP/ $\alpha$ -MoO<sub>3</sub> parallel-plate structures, *Appl. Phys. Lett.* **120**, 112204 (2022).
- [52] Z. X. Wang, Z. L. Shen, D. H. Han, Y. F. Xu, M. Becton, X. Q. Wang, L. Y. Zhang, and X. F. Chen, Significant enhancement of near-field radiative heat transfer between black phosphorus-covered hyperbolic metamaterial, *J. Appl. Phys.* **128**, 065109 (2020).
- [53] K. Chaudhary, M. Tamagnone, M. Rezaee, D. K. Bediako, A. Ambrosio, P. Kim, and F. Capasso, Engineering phonon polaritons in van der Waals heterostructures to enhance in-plane optical anisotropy, *Sci. Adv.* **5**, eaau7171 (2019).
- [54] C. L. Zhou, X. H. Wu, Y. Zhang, and H. L. Yi, Super-Planckian thermal radiation in borophene sheets, *Int. J. Heat Mass Transfer* **183**, 122140 (2022).
- [55] C. L. Zhou, X. H. Wu, Y. Zhang, H. L. Yi, and D. Novko, Near-field thermal radiation of germanium selenide single layer, *Phys. Rev. Materials* **5**, 124005 (2021).
- [56] C. L. Zhou, Z. Torbatian, X. H. Wu, Y. Zhang, H. L. Yi, and D. Novko, Tunable Near-Field Radiative Effect in a T<sub>d</sub>-WTe<sub>2</sub> Single Layer, *Phys. Rev. Applied* **17**, 014044 (2022).
- [57] H. Hajian, I. D. Rukhlenko, G. W. Hanson, T. Low, B. Butun, and E. Ozbay, Tunable plasmon-phonon polaritons in anisotropic 2D materials on hexagonal boron nitride, *Nanophotonics* **9**, 3909 (2020).
- [58] See Supplemental Material at <http://link.aps.org/supplemental/10.1103/PhysRevMaterials.6.075201> for (1) expression for transmission and reflection coefficients of the heterostructure composed of anisotropic 2D material and hyperbolic film, (2) plasmon dispersion formulation for this heterostructure, (3) the optical properties of materials, and (4) the effect of *h*BN film thickness on ESPPP mode, which includes Refs. [59–65].
- [59] Kotov and Y. E. Lozovik, Hyperbolic hybrid waves and optical topological transitions in few-layer anisotropic metasurfaces, *Phys. Rev. B* **100**, 165424 (2019).
- [60] M. J. He, H. Qi, Y. T. Tao, Y. J. Zhao, and M. Antezza, Magnetoplasmon-surface phonon polaritons coupling effects in radiative heat transfer, *Opt. Lett.* **45**, 5148 (2020).
- [61] M. J. He, H. Qi, Y. T. Tao, Y. J. Zhao, Y. Zhang, J. D. Shen, and M. Antezza, Radiative thermal switch driven by anisotropic black phosphorus plasmons, *Opt. Express* **28**, 26922 (2020).
- [62] J. S. Gomez-Diaz, M. Tymchenko, and A. Alù, Hyperbolic metasurfaces: surface plasmons, light-matter interactions, and physical implementation using graphene strips, *Opt. Mater. Express* **5**, 2313 (2015).
- [63] P. Yeh, Electromagnetic propagation in birefringent layered media, *J. Opt. Soc. Am.* **69**, 742 (1979).
- [64] L. Lu, B. Zhang, H. Ou, B. W. Li, J. L. Sun, Z. X. Luo, and Q. Cheng, Enhanced near-field radiative heat transfer between graphene/*h*BN systems, *Small* **18**, 2108032 (2019).
- [65] X. J. Yi, L. Y. Zhong, T. B. Wang, W. X. Liu, D. J. Zhang, T.B.Yu, Q. H. Liao, and N. H. Liu, Near-field radiative heat transfer between hyperbolic metasurfaces based on black phosphorus, *Eur. Phys. J. B* **92**, 217 (2019).
- [66] S. A. Biehs, F. S. S. Rosa, and P. Ben-Abdallah, Modulation of near-field heat transfer between two gratings, *Appl. Phys. Lett.* **98**, 243102 (2011).
- [67] Y. H. Kan, C. Y. Zhao, and Z. M. Zhang, Near-field radiative heat transfer in three-body systems with periodic structures, *Phys. Rev. B* **99**, 035433 (2019).
- [68] R. Messina, P. Ben-Abdallah, B. Guizal, M. Antezza, and S.-A. Biehs, Hyperbolic waveguide for long-distance transport of near-field heat flux, *Phys. Rev. B* **94**, 104301 (2016).
- [69] Z. Yuan, R. K. Chen, P. N. Li, A. Y. Nikitin, R. Hillenbrand, and X. L. Zhang, Extremely confined acoustic phonon polaritons in monolayer-*h*BN/metal heterostructures for strong light-matter interactions, *ACS Photonics* **7**, 2610 (2020).
- [70] N. Rivera, T. H. Christensen, and P. Narang, Phonon polaritonics in two-dimensional materials, *Nano Lett.* **19**, 2653 (2019).
- [71] R. Petersen, T. G. Pedersen, and F. J. García de Abajo, Nonlocal plasmonic response of doped and optically pumped graphene, MoS<sub>2</sub>, and black phosphorus, *Phys. Rev. B* **96**, 205430 (2017).
- [72] S. Dai, Z. Fei, Q. Ma, A. S. Rodin, M. Wagner, A. S. McLeod, M. K. Liu, W. Gannett, W. Regan, K. Watanabe, T. Taniguchi, M. Thiemens, G. Dominguez, A. H. Castro Neto, A. Zettl, F. Keilmann, P. Jarillo-Herrero, M. M. Fogler, and D. N. Basov, Tunable phonon polaritons in atomically thin van der Waals crystals of boron nitride, *Science* **343**, 1125 (2014).
- [73] P. Li, I. Dolado, F. J. Alfaro-Mozaz, A. Yu. Nikitin, F. Casanova, L. E. Hueso, S. Vélez, and R. Hillenbrand, Optical nanoimaging of hyperbolic surface polaritons at the edges of van der Waals materials, *Nano Lett.* **17**, 228 (2017).
- [74] X. H. Wu and C. J. Fu, Hyperbolic volume and surface phonon polaritons excited in an ultrathin hyperbolic slab: Connection of dispersion and topology, *Nanosc. Microsc. Therm.* **25**, 64 (2021).
- [75] G. W. Hu, A. Krasnok, Y. Mazor, C. W. Qiu, and A. Alù, Moiré hyperbolic metasurfaces, *Nano Lett.* **20**, 3217 (2020).
- [76] G. W. Hu, Q. D. Ou, G. Y. Si, Y. J. Wu, J. Wu, Z. G. Dai, A. Krasnok, Y. Mazor, Q. Zhang, Q. L. Bao *et al.*, Topological polaritons and photonic magic angles in twisted  $\alpha$ -MoO<sub>3</sub> bilayers, *Nature (London)* **582**, 209 (2020).
- [77] M. Y. Chen, X. Lin, T. H. Dinh, Z. R. Zheng, J. L. Shen, Q. Ma, H. S. Chen, P. Jarillo-Herrero, and S. Y. Dai, Configurable phonon polaritons in twisted  $\alpha$ -MoO<sub>3</sub>, *Nat. Mater.* **19**, 1307 (2020).
- [78] S. Dai, Q. Ma, M. K. Liu, T. Andersen, Z. Fei, M. D. Goldflam, M. Wagner, K. Watanabe, T. Taniguchi, M. Thiemens *et al.*, Graphene on hexagonal boron nitride as a tunable hyperbolic metamaterial, *Nat. Nanotechnol.* **10**, 682 (2015).
- [79] R. J. Koch, Th. Seyller, and J. A. Schaefer, Strong phonon-plasmon coupled modes in the graphene/silicon carbide heterosystem, *Phys. Rev. B* **82**, 201413(R) (2010).
- [80] R. Messina, J. P. Hugonin, J. J. Greffet, F. Marquier, Y. D. Wilde, A. Belarouci, L. Frechette, Y. Cordier, and P. Ben-Abdallah, Tuning the electromagnetic local density of states in graphene-covered systems via strong coupling with graphene plasmons, *Phys. Rev. B* **87**, 085421 (2013).